ADVANCED MATERIALS
www.advmat.de

Sampling the Materials Space for Conventional Superconducting Compounds

*Tiago F. T. Cerqueira, Antonio Sanna, and Miguel A. L. Marques**

A large scale study of conventional superconducting materials using a machine-learning accelerated high-throughput workflow is performed, starting by creating a comprehensive dataset of around 7000 electron–phonon calculations performed with reasonable convergence parameters. This dataset is then used to train a robust machine learning model capable of predicting the electron–phonon and superconducting properties based on structural, compositional, and electronic ground-state properties. Using this machine, the transition temperatures (T_c) of approximately 200 000 metallic compounds are evaluated, all of which are on the convex hull of thermodynamic stability (or close to it) to maximize the probability of synthesizability. Compounds predicted to have T_c values exceeding 5 K are further validated using density-functional perturbation theory. As a result, 541 compounds with T_c values surpassing 10 K, encompassing a variety of crystal structures and chemical compositions, are identified. This work is complemented with a detailed examination of several interesting materials, including nitrides, hydrides, and intermetallic compounds. Particularly noteworthy is $LiMoN_2$, which is predicted to be superconducting in the stoichiometric trigonal phase, with a T_c exceeding 38 K. $LiMoN_2$ has previously been synthesized in this phase, further heightening its potential for practical applications.

1. Introduction

Superconducting materials are used in a growing number of applications crucial to technological, societal, and economical development. These include low magnetic field systems like cables, transformers, and motors, qubits for quantum computers and, more significantly, high field devices for medical diagnostic, accelerators in particle physics and plasma confinement for fusion technology.[1,2] Hundreds of superconducting material families have been discovered, among which the copper-oxides[3] with critical temperatures (T_c) exceeding 100 K, MgB_2 with T_c=39 K,[4] the ferro-pnictides reaching a T_c of 55 K,[5,6] and more recently the high pressure hydrides,[7–10] with critical temperatures close to room values.

It is then, at a first sight, surprising that some of the largest experiments in physics, like the Large-Hadron Collider at CERN or the International Thermonuclear Experimental Reactor (our biggest hope of developing a source of clean and nearly infinite energy), rely on superconductors — Nb–Ti alloys and Nb_3Sn — that were developed half a century ago and were already in use in the 1970s.[11] The reason is that, despite their remarkable superconducting properties, most high-Tc materials are extremely brittle and therefore poorly suited to make the many kilometers of wire or tape required.[2,12] In addition, cuprates suffer from the grain boundary problem, which makes the construction of long stable cables complex and expensive. In contrast, Nb–Ti forms ductile alloys, which are well suitable for fabricating Cu-stabilized multifilamentary conductors, but have a low critical temperature. However, Nb is an expensive chemical element of limited availability.

In view of this situation, it is urgent to discover new industry-friendly materials that may resolve, or at least alleviate, the current dependence of the industry on Nb-based superconductors. Over the last years several high-profile projects were aimed to discover new superconductors, including a large-scale four-year proposal financed by the Japanese government.[13] The overwhelming majority of the candidate systems turned out to be non-superconducting, and only 100 new superconducting materials were found, mostly iron-based or analogous to them. This gives a clear indication of the low time- and cost-effectiveness of the

T. F. T. Cerqueira
CFisUC
Department of Physics
University of Coimbra
Rua Larga, Coimbra 3004-516, Portugal
A. Sanna
Max-Planck-Institut für Mikrostrukturphysik
Weinberg 2, D-06120 Halle, Germany
M. A. L. Marques
Research Center Future Energy Materials and Systems of the University Alliance Ruhr
Faculty of Mechanical Engineering
Ruhr University Bochum
Universitätsstraße 150, D-44801 Bochum, Germany
E-mail: miguel.marques@rub.de

The ORCID identification number(s) for the author(s) of this article can be found under https://doi.org/10.1002/adma.202307085

DOI: 10.1002/adma.202307085

traditional experimental trial-and-error search for superconductors.

A targeted approach where synthesis is only attempted following an accurate theoretical prediction could be more efficient. This is possible for conventional superconductors, that are well understood, and for which predictive quantitative theories exist.[14–18] Unfortunately search has been mostly focused on selected chemical compositions and small families of compounds,[10,19–23] while very few large scale studies of superconductors can be found in the literature. In 2022, Hoffmann et al. studied the whole family of antiperovskites,[24] performing electron-phonon calculations for more than 400 compounds. This was followed by a similar work on full-Heusler materials comprising more than 1000 candidate systems, and discovering a total of eight hypothetical materials with critical temperatures above 10 K.[25] In spite of relatively large number of chemical compositions studied, these works were however strongly limited in terms of the possible crystal structures.

In a seminal work, Choudhary and Garrity[26] overcame this limitation by devising a multi-step, machine-learning accelerated workflow for discovering conventional superconductors. They conducted electron–phonon coupling calculations for 1058 compounds with varying structures and chemical compositions, leading to the identification of 105 dynamically stable materials with T_c above 5 K, but only 17 with T_c above 10 K and having distances to the hull of stability smaller than 50 meV/atom. The work of Choudhary and Garrity used a small $2 \times 2 \times 2$ $q-$point mesh to generate data for training, but $k-$ and $q-$grids were then converged for the best candidates predicted by the machine. A similar approach was then also applied to 2D systems, unveiling 34 compounds with a transition temperature above 5 K.[27] We strongly believe that this approach is the right path to follow, because it targets the complete space of possible materials.

There have been a few other machine learning studies of superconductors,[28–30] most of them based on the SuperCon database.[31] Unfortunately, SuperCon contains solely the composition of the compound and not its crystal structure, limiting the use of machine learning to simple compositional models. (Note that recently a subset of the SuperCon structures has been identify,[32] alleviating this shortcoming.) Furthermore, the compounds present in SuperCon are considerably biased towards cuprates and iron-based materials, making the training of general models difficult.

In this work, we take a step further by creating a larger and better converged dataset of calculated electron–phonon and superconducting properties that is used to train a *robust* machine-learning model for predicting the transition temperature of conventional superconductors. This model is then used to sieve through almost 200 000 compounds to uncover a large number of conventional superconductors with high-T_c.

The remainder of this article is structured as follows: Section 2 explains our general strategy and workflow. The training dataset is described and analyzed in Section 3, providing insights about the properties of conventional superconductors and their statistical distribution. Section 4 is devoted to our predictions, presenting the most interesting compounds we have found and providing a full characterization of a few noteworthy materials. Finally, we present our conclusion in Section 5.

2. Strategy and Workflow

Our search workflow is summarized in **Figure 1** and commences with the creation of a large dataset of electron–phonon calculations. The selection of materials for this dataset is a critical step that requires careful consideration. On the one hand, the choice should aim to minimize possible biases in the representation of chemical elements and crystal structures, ensuring a diverse and representative sample. On the other hand, the computational effort required for electron–phonon calculations increases steeply with the number of atoms in the unit cell, necessitating thorough assessment of computational feasibility.

We start with the stable or nearly stable compounds (below 50 meV/atom from the convex hull of thermodynamic stability) from the Alexandria database of Refs. [33, 34]. We discarded semiconductors, insulators, and any material with nonzero magnetic moments as these should not host a stable superconducting state with large critical temperature. Also, metals with a very low density of states at the Fermi level (DOS(E_F)) are less relevant and were filtered out.

In addition to these, somehow straightforward, selection criteria, we added a further filter by including only materials with an estimated Debye temperature (Θ_D) above a cutoff of 300 K. Although there is no simple proportionality between the Debye temperature and T_c, it is a fact that the best superconductors have relatively large phonon frequencies. As the Alexandria dataset does not include the values for the Debye temperature, these were estimated using a crystal-graph neural network (see Section 6). We note that the cutoffs in DOS(E_F) and Θ_D were already used in Refs. [26,34].

For numerical efficiency reasons, we also limited the training set to compounds with $\leqslant$8 atoms in the primitive unit cell, and space group number $\geqslant$100 (including most tetragonal, and all trigonal, hexagonal, and cubic lattices, but excluding the orthorhombic, monoclinic, and triclinic systems).

Subsequently, the entries were arranged based on Pareto fronts within the DOS(E_F) and Θ_D parameter space, and the calculation of the electron–phonon interaction was performed with density-functional perturbation theory[35–37] (DFPT) in that specified sequence (refer to Section 6). To increase the diversity of the dataset, we added entries with few atoms in the unit cell ($\leqslant$5) from higher Pareto fronts. This comprises a space of 23410 materials, out of which we performed a total of 6545 DFPT calculations. Finally, we also included the 50 materials already calculated by some of us in Ref. [34], and the datasets of Heuslers from Ref. [25] and of inverted perovskites from Ref. [24] (295 and 168 materials, respectively). These later two were originally calculated with the LDA functional[38] and with k and q-point sets specifically chosen for those crystal structures. In order to make the data compatible with our current approach, the ground-state and the electron–phonon coupling constants were recalculated with the parameters presented in Section 6. Note that a table containing a summary of all our DFPT calculations can be found in the Supporting Information (SI).

Our training dataset (DS-A) contains results for 7217 dynamically stable materials, of which 2426 have a $T_c^{\text{Allen-Dynes}}$ (T_c estimated with the Allen-Dynes formula[39]) larger than 1 K, 773 larger than 5 K, and 272 larger than 10 K. This dataset, analyzed in detail in Section 3, was used to train machine-learning

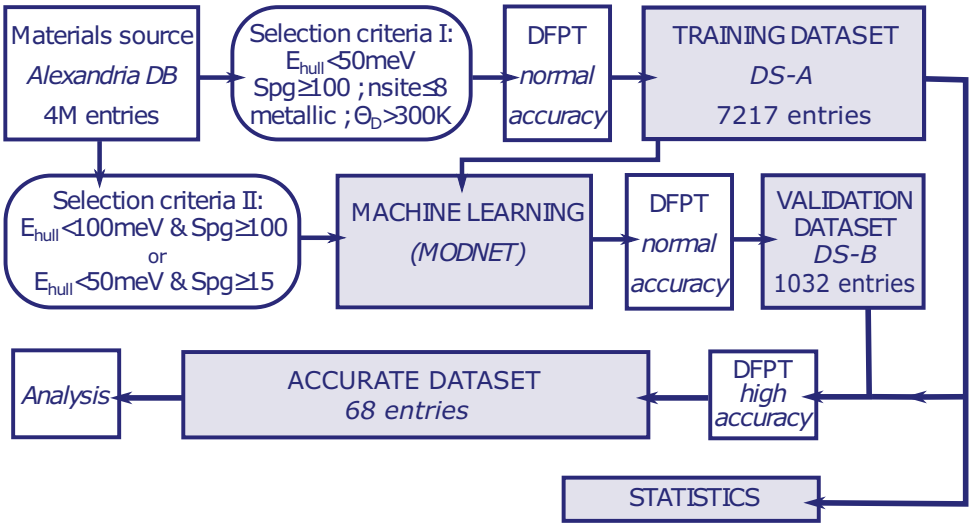

Figure 1. Sketch of our search workflow. We start from a large database of crystal structures and Density Functional Theory calculations. From this we select and compute (via DFPT with *normal* precision) a training database (DS-A) whose superconducting properties are computed from first principles. DS-A is used for training a machine learning model. The machine is used to identify promising materials, which are simulated and included into a second dataset (DS-B). We used the materials in DS-A for a statistical study (as these are not biased by the machine-learning model) and select the best systems among all the computed materials (DS-A + DS-B) for a more detailed analysis.

models for predicting the logarithmic average of the phonon frequencies ω_{log}, the electron-phonon coupling constant λ, and the superconducting transition temperature. The models considered structural, compositional, and ground-state features, and we employed MODNET[40] and ALIGNN[41] using various inputs, outputs, and training strategies. Our most successful network was a MODNET model using as input features the structure and composition of the compound together with DOS(E_F) and Θ_D (see Section 6). The output was the vector composed of ω_{log}, λ, and T_c and the cost function was the linear combination (with equal weights) of the error in these three quantities.

We applied this machine to predict the transition temperature of three further datasets, that we refer together as our B dataset (DS-B). As before, we excluded magnetic and semiconducting compounds. We note that our model gives us access to two different estimations of T_c, one predicted directly and the other calculated from the predicted values of λ and ω_{log}. In order to minimize the number of false negatives, we selected for electron–phonon calculations compounds for which at least one of the two predicted values of T_c was larger than 5 K.

(i) First, we selected metals with a maximum of eight atoms in the primitive unit cell, including trigonal, hexagonal, and cubic systems, present in the database[33,34] within 50 meV/atom from the convex hull (amounting to a material space of 108771 entries). We note that our DS-A is actually a subset of this set of materials. The only difference is that here, we removed the restrictions on the minimum DOS(E_F) and Θ_D. We obtained with DFPT 198 new dynamically stable compounds, of which 106 had a transition temperature above 5 K. This resulted in a success rate of 54%.

(ii) In this case, we relaxed the thermodynamic stability constrain, and allowed for compounds with a maximum of five atoms in the primitive unit cell, including trigonal, hexagonal, and cubic systems, present in the database[33,34] between 50 and 100 meV/atom from the convex hull. This amounted to a material space of 65288 compounds. We found 721 dynamically stable phases, from which 549 had a transition temperature above 5 K. This resulted in a success rate of 76%.

(iii) To investigate lower symmetry compounds, we selected orthorhombic and tetragonal compounds with a maximum of five atoms in the primitive unit cell present in the database[33,34] within 50 meV/atom from the convex hull. This amounted to a material space of 17469 compounds. We found 114 dynamically stable phases, of which 72 had a transition temperature above 5 K. This resulted in a success rate of 63%.

Together, we searched a material space of 191528 compounds with our machine learning model, performing DFPT calculations for 1032 materials. The results showed an average success rate to find compounds with $T_c > 5$ K of 70%. We note that in the initial dataset DS-A only around 10% of the compounds were found to have $T_c > 5$ K, proving the efficiency of our approach. Altogether, the utilization of the machine learning model resulted in a 23-fold acceleration of the search process, factoring in the time required for training set creation.

We estimated the precision on T_c of our machine in DS-B with a mean of $T_c = 7.63$ K, obtaining a mean absolute error of $T_c = 2.94$ K. To put this figure into perspective, we can consider two hypothetical machines: i) A machine that predicts $T_c = 0$ K for all entries would yield a mean absolute error of 7.63 K, which corresponds to the mean value of the test set; ii) Alternatively, a machine that predicts T_c to be the mean of the values in the training set (1.72 K) would result in a mean absolute error of 6.07 K. For comparison, the machine in Ref. [26] had an error of 1.84 K for a mean value of the training set of 2.72 K. We attribute this

notable improvement to the substantial expansion of the training set, which was around ten times larger than the dataset used in Ref. [26].

We note that our value is just an estimation, as DS-B is biased by the choice by the machine model of systems with T_c larger then 5 K. A more statistically robust estimate of the error is the cross-validation error during training. Our best machine predicted, at the same time, the transition temperature, ω_{log}, and λ. As such, the cost function used to train the machine was the sum, with equal weights, of the errors in the three quantities. The calculated individual contributions for the cross-validation error are 1.212 ± 0.085 for T_c 0.105 ± 0.003 for λ, and 23.166 ± 0.994 for ω_{log}. As we can see, the cross-validation values are lower than the errors obtained for DS-B, which is understandable since the target distribution is skewed towards higher values of λ, ω_{log} and T_c. While we acknowledge that the dataset DS-B is biased as it was selected by the machine, we maintain the belief that the error in this dataset yields valid insights, particularly in the region of higher T_c that is of greatest interest to us. As a result, our model can now make robust predictions of superconducting compounds solely based on their structural, compositional, and ground-state properties.

The described workflow, consisting of multiple precision steps, may appear complicated. However, given the inherent computational complexity involved in the search for superconductors, it appears to us as the most viable approach for accelerating the discovery process.

3. Statistics

In this section, our focus lies on the training dataset (DS-A). The quality of our ab initio simulations enables us to conduct a meaningful statistical analysis of this set. Our primary objective is to identify the key properties associated with high T_c. Most importantly, w e aim at estimating the rarity of finding conventional superconductors with a given critical temperature. Here, w e do not include the materials found by machine-learning in order to reduce the bias in the statistical distributions. The DS-A set may still possess some bias due to our initial selection process, with the purpose of excluding non-superconducting systems and materials with excessive computational cost. However, these are relatively minor issues and, we believe, that the dataset still holds valuable statistical information.

3.1. Chemical Space

In **Figure** 2a we plot the distribution of chemical elements in our DS-A. The boxes in gray represent either chemical elements for which we did not have pseudopotentials available or the rare gases that do not form metallic compounds at ambient conditions. We would also like to note that we only have few compounds with Ir in DS-A due to the problems with its pseudopotential mentioned in Section 6. In general, the number of occurrences decreases with the period. The exceptions are the 3*d* elements Cr, Mn, Fe, etc. that have the tendency to form magnetic compounds that were removed from the dataset. Non-metals are also much less represented than metals, as most systems in DS-A are intermetallic compounds. Also, we note the scarcity of compounds with heavy alkali and alkali earth elements.

If we now look at the distribution of the chemical elements present in compounds having $T_c^{\text{Allen-Dynes}} > 5$ K we obtain a completely different picture. As expected, many superconducting compounds contain hydrogen. However, the largest fraction of superconducting compounds include early transition metals with a peak appearance of Nb and Ti compounds. Moreover, the ideal group for superconductivity appears to be group VI, with 30% of Cr-, 18% of Mo-, and 16% of W-compounds having $T_c^{\text{Allen-Dynes}} > 5$ K, followed by group VII (Mn, Tc, Re) and group V (V, Nb, Ta). However, the latter group has the advantage of being less magnetic so superconductivity does not have to compete with disrupting effects as spin fluctuations (which we do not consider in this work). The occurrence of noble metals and non-metals is very much reduced. However, as we will see in the following, while not statistically prevalent, we do find compounds with extreme values of T_c including these elements. Another interesting fact relates to the second row of the periodic table: we find an increase of high-temperature superconducting systems going from B to C, arriving at a maximum for N (17% of its compounds having $T_c^{\text{Allen-Dynes}} > 5$ K), and then decreasing for O and F. This behavior is not mirrored in the third row where the ideal element for superconductivity is sulphur (19% with $T_c^{\text{Allen-Dynes}} > 5$ K). This indicates that nitrogen and sulphur might be very favorable targets for the design of thermodynamically stable high-T_c conventional superconductors, better than the well-known B and C.

The presence of non-metallic elements is, at room pressure, linked with the formation of strong covalent bonds. Often this type of bonds leads to insulating or semiconducting systems. However, when covalent bonds occur in metallic compounds they may lead to strong electron–phonon coupling (if the Fermi level states are part of those bonds). This mechanism is responsible for superconductivity in MgB_2 as discussed in Pickett's seminal paper.[42] Likely this is the only conventional mechanism which is able to support high critical temperatures at room pressure, therefore the evidence that H, N, C, O containing materials lead to the highest T_c.

3.2. Superconducting Properties

In **Figure** 3, we plot histograms of the electron–phonon and superconducting properties, as calculated in our DS-A dataset. Due to the large amount of compounds, the histograms are very smooth, in contrast to results for Heusler or anti-perovskite compounds only.[24,25]

In panel (a) we see that the distribution of values of λ is, as expected, very asymmetric, with a maximum value at around 0.25 and with a fat tail that extends well beyond $\lambda = 1$ (see inset). The mean value of the distribution $\lambda_{mean} = 0.37$) is in very good agreement with the mean value found for Heuslers ($\lambda_{mean} = 0.30$) and anti-perovskites ($\lambda_{mean} = 0.36$). Surprisingly, the histogram can be fit by a lognormal distribution, allowing us to easily calculate probabilities. Note that, strictly speaking, these are conditional probabilities reflecting any residual bias present in the choice of materials contained in the dataset of Ref. [33, 34], and of our choices detailed in Section 2. With this in mind, we find that the probability to find a material with λ greater than 0.5 is 19.6%,

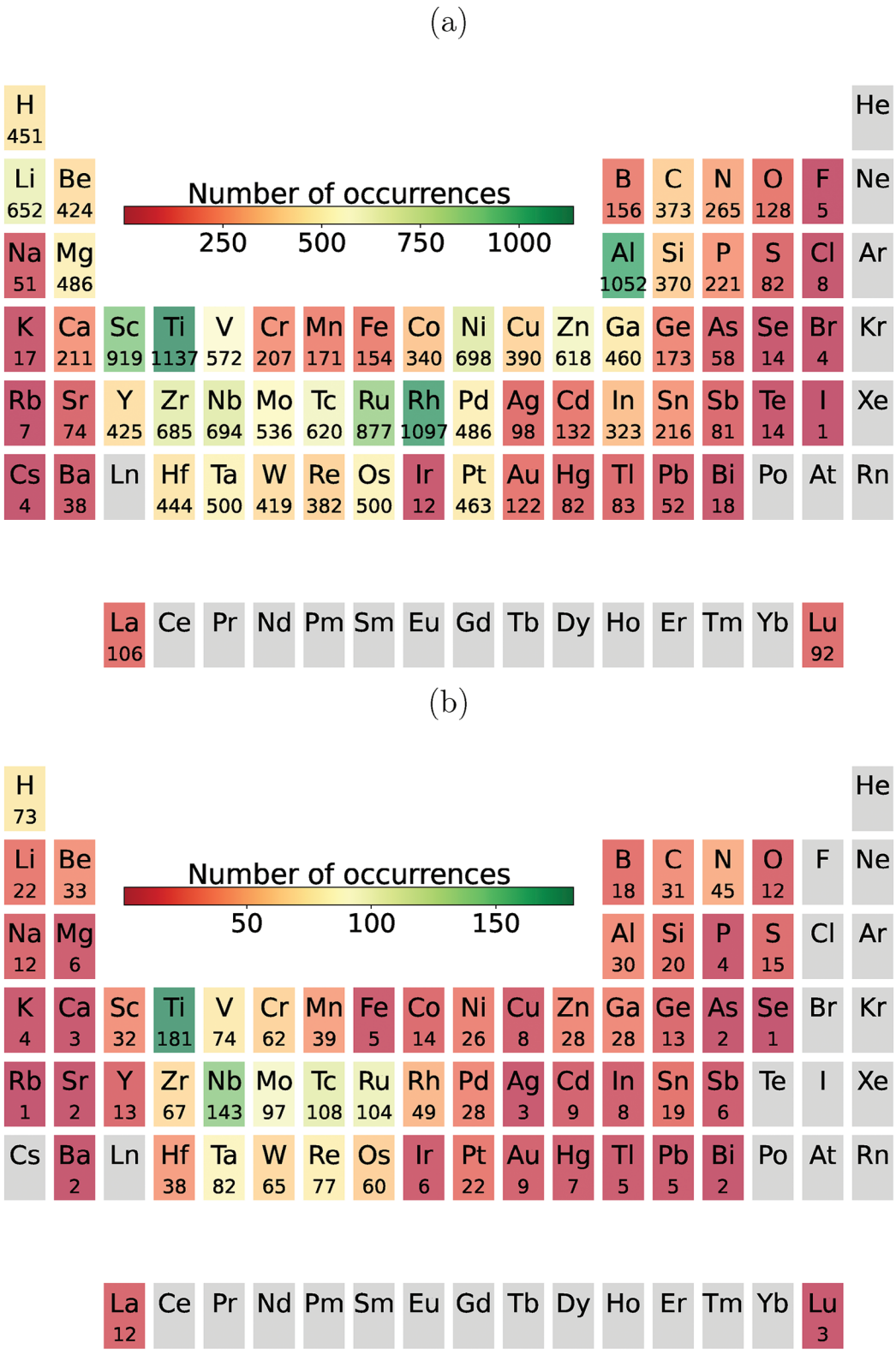

Figure 2. Periodic table with the number of occurrences of each chemical for a) all compounds in DS-A and b) compounds in DS-A with a $T_c^{\text{Allen-Dynes}}$ larger than 5 K.

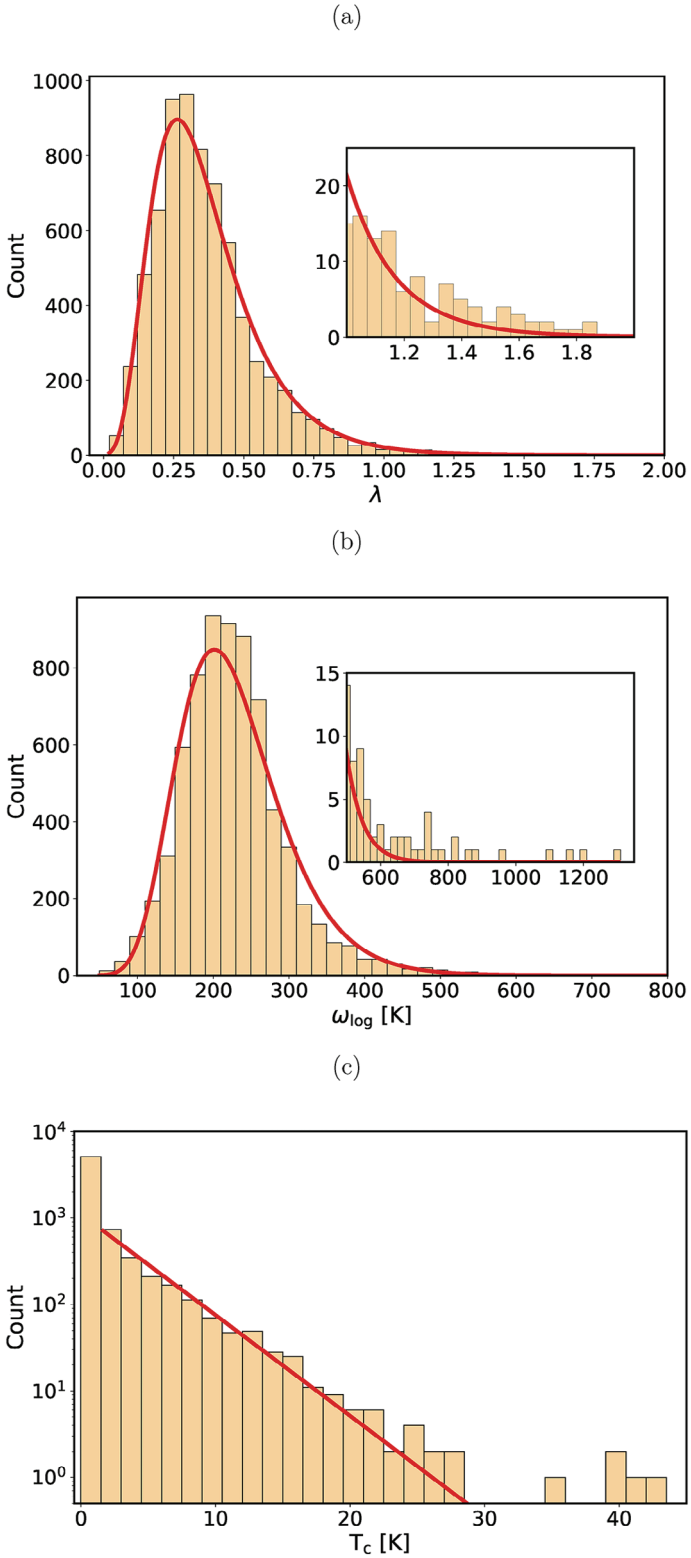

Figure 3. a) Histogram of the electron–phonon coupling constant λ with bins of width 0.05. The red curve is a fit to a lognormal distribution $f(x, s) = \frac{1}{sdx\sqrt{2\pi}} \exp(-\frac{\log^2(y)}{2s^2})$, with $y = (x - \bar{x})/d$, yielding the parameters $s = 0.433$, $\bar{x} = -0.0618$, and $d = 0.392$; b) Histogram of the logarithmic averaged phonon frequency $\omega_{\log}$ with bins of width 20 K; The red curve is a fit to a lognormal distribution with parameters $s = 0.276$, $\bar{x} = -26.3$, and $d = 246$; c) Histogram of the values of the transition temperature T_c with bins of width 1.5 K. Note the logarithmic scale on the y-axis. The red curve is a fit, performed for entries with $T_c > 1.5$ K, of an exponential distribution $\exp(-y)/d$, yielding $\bar{x} = 1.50$ and $d = 3.72$. The fits were performed with SCIPY.[43]

greater than 0.75 is 4.5%, and greater than 1.0 is 1.0%. We note that if we zoom the plot in the region of the tail, we find many more compounds with large values of λ than expected from the distribution. However, we cannot use this fact as an evidence for the existence of a fat, Pareto tail, as many of these large values of λ come from false positive materials with soft modes.

The histogram of $\omega_{\log}$ is shown in Figure 3b. As expected by the distribution of atomic masses, almost all materials exhibit $\omega_{\log}$ between around 100 and 400 K, with a maximum of around 200 K. The mean of the distribution is 229 K, again comparing well to the one of Heusler (190 K) and anti-perovskite (234 K) compounds. Not surprisingly, the rare cases of very large $\omega_{\log}$ shown in the inset of Figure 3b are all compounds with light atoms like H. This distribution can also be fitted by a lognormal curve, although the quality of the fit is somewhat inferior to the one of λ. This may be related to the cutoff in Θ_D used to select the materials, that could lead to a artificial decrease of materials with small $\omega_{\log}$.

Finally, in panel (c) of Figure 3, we depict the distribution of values of T_c calculated from the Allen-Dynes formula. We can observe that the large majority of compounds is not superconducting, or exhibits a very small (<1.5 K) transition temperature. For higher T_c the number of compounds decreases exponentially until around 20–25 K, but a few outliers can be found with higher transition temperatures. Unfortunately, most of these outliers turn out to be false positives with soft phonon modes. These results are very much in line with the old assumption that conventional superconductivity is limited to about 30 K. In fact, while nothing prevents phononic superconductors to reach much higher critical temperatures, these cases appear to be extremely rare, at least within the restriction of being at ambient pressure, excluding anisotropy effects and considering only systems that are stable or close to thermodynamic stability.

The exact probabilities of higher critical temperatures are difficult to estimate. In our DS-A set only two exceed 40 K (with our Eliashberg estimation), which leads to a probability of 0.03%. Using the lognorm fit of the electron–phonon coupling and of the phonon frequencies, and assuming the values of the three parameters of the Allen-Dynes equation to be uncorrelated, the Allen-Dynes formula predicts that the decrease of probability with T_c is almost exponential. However the lognorm fit is not very precise at extreme values (as shown by the insets in Figure 3) and extreme values of T_c do arise from these deviations from the exponential tail.

On the other hand, we find a significant number of superconductors in the 20 to 30 K range of T_c, in the order of 0.2% to 0.5% of the materials in DS-A. Superconductors within this range of T_c may not represent a technological game changer but could still be valuable for specific applications if superconductivity is accompanied by other desirable properties, like abundance of the atomic species, ductility, and high critical fields and currents.

4. Extreme Compounds

As discussed in Section 2 the training dataset DS-A is used to build machine learning models and predict new superconductors. The most interesting predictions (following the criteria detailed in Section 2) are validated from first principles and collected into the dataset DS-B.

In this section, we explore all compounds in DS-A and DS-B that exhibit exceptionally high values of T_c. For our analysis of specific materials, we rely on calculations conducted using the high-precision setting (see Section 6), and we determine T_c using the isotropic Eliashberg equation. It is worth noting that the high-precision calculation involves substantial computational effort. In addition, we have chosen three cases of extreme interest to be analyzed by a cutting-edge SCDFT methodology, including anisotropy and ab initio Coulomb interactions.

Some of the compounds in DS-A, such as KB_6,[45] NbC,[46] MgB_2,[4] NbB_2, and TaB_2,[47] RuO_2,[26] etc., are known superconductors or have already been proposed in the literature as superconductors. On the other hand, some of the materials in DS-B, once computed with the high-precision setting, turn out to be unstable or non-superconducting. A selection of the most promising compounds, that we found with the highest values of T_c or including chemical elements unusual in conventional superconductors, is listed in **Table 1**. This table includes a set of materials that our methodology has predicted that could be synthesizable valuable superconductors. In the sections below, we discuss these materials grouping them into families. Further information concerning their electronic and phononic band structures and the electron-phonon coupling is given in the Supporting Information.

4.1. Nitrides

Table 1 contains a large number of nitride compounds with high-T_c. Above 20 K, we find $LiMoN_2$ (at an incredible $T_c^{\text{Eliashberg}}$ = 46 K), $ScMoN_2$ ($T_c^{\text{Eliashberg}}$ = 30 K), and $LiTcN_2$ ($T_c^{\text{Eliashberg}}$ = 28 K). Due to the relevance of this finding, $LiMoN_2$ is studied in detail in the following. Additionally, we have identified a series of systems with similar chemical compositions that crystallize in the γ-$LiBO_2$ (chalcopyrite) structure. Several nitrides adopting this structure have been synthesized in the past, including $MgGeN_2$,[48] $CaGeN_2$,[49] $LiPN_2$,[50] and $NaPN_2$.[51] Furthermore, other $A^{II}B^{IV}N_2$ compounds have been produced in the related β-$NaFeO_2$ phase, such as $BeSiN_2$,[52] $MgSiN_2$,[53] $MgGeN_2$,[53] and $ZnGeN_2$.[54]

The nitride chalcopyrite compound with the highest transition temperature that we have discovered is $LiTcN_2$. While this compound is thermodynamically stable, its practical applications are limited due to the presence of the radioactive chemical element Tc. Interestingly, the Fermi energy resides in a valley of the density of states, suggesting that T_c can be enhanced through doping with either electrons or holes. The electron–phonon coupling constant λ is calculated to be 1.33, with the majority of the contribution stemming from the acoustic and first optical phonons below 24.8 meV. With an electronic logarithmic average $\omega_{\log}$ of 241 K, this results in a critical temperature of $T_c^{\text{Eliashberg}}$ = 28 K.

It is worth mentioning that $LiMoN_2$ is also dynamically stable in the chalcopyrite structure, with an energy only 56 meV/atom above the convex hull. However, the superconducting critical temperature decreases compared to the trigonal phase. For $LiMoN_2$ in the chalcopyrite structure, we find $T_c^{\text{Eliashberg}}$ = 22 K,

Table 1. Calculated superconducting properties with the high-precision settings. We present the chemical formula, the space group number (Spg), the number of atoms in the primitive unit cell (NSites), the distance to the convex hull E_{hull} (calculated as in Ref. [44], in meV/atom), ω_{log} (in K), λ, and the transition temperature calculated from the solution of the isotropic Eliashberg equation ($T_c^{Eliashberg}$ in K). The transition temperature was obtained with $\mu^* = 0.10$.

Formula	Spg	NSites	E_{hull}	ω_{log}	λ	$T_c^{Eliashberg}$
$LiMoN_2$	160	4	8	268.6	1.777	46.3
$LiPdH_2$	166	4	101	531.8	0.981	43.2
HPd	225	2	35	342.5	1.239	37.4
$LiTcN_2$	122	8	0	241.4	1.325	28.4
$NaTcN_2$	122	8	0	260.7	1.211	27.4
ZrH_3	139	4	94	363.4	0.967	24.9
V	229	1	5	204.6	1.329	24.9
Nb_3Zn	223	8	82	113.1	2.390	24.7
Cr_4ReW	216	6	40	189.9	1.414	24.3
TiV_2	139	3	41	213.6	1.258	24.0
TiV	129	4	46	190.9	1.369	24.0
$LiMoN_2$	122	8	56	292.0	0.990	22.4
$TiNb_3$	123	4	32	150.3	1.556	21.9
$ZrTc_2$	227	6	29	149.9	1.443	20.2
Ti	225	1	62	204.9	1.117	19.7
$LiVRu_2$	225	4	39	149.4	1.419	19.3
Cr_3Os	223	8	21	239.7	0.987	19.1
MgB_2	191	3	0	725.1	0.594	18.9
NbC	225	2	47	330.3	0.835	18.5
$TiNbV_4$	216	6	36	148.3	1.275	17.7
Cr_2Re	164	3	41	252.2	0.895	17.1
Nb	229	1	29	147.1	1.248	17.0
$ScMoC_2$	166	4	49	288.0	0.864	16.9
MoH	225	2	0	241.4	0.931	16.8
KB_6	221	7	0	803.3	0.559	16.8
Ti_3Te	223	8	56	186.8	1.041	16.3
V_6CoSi	200	8	23	262.9	0.849	16.2
RbB_6	221	7	28	811.2	0.548	16.0
TaB_2	191	3	0	297.0	0.816	15.4
CrH	225	2	0	310.6	0.767	15.3
Zr	225	1	40	132.9	1.236	14.7
Ti_2H	166	3	45	171.1	1.005	14.1
Ti_2W	164	3	22	196.5	0.898	13.4
ZrN	225	2	0	377.2	0.667	13.3
TaNb	221	2	6	162.1	1.001	13.3
Ti_2Tc	139	3	9	211.5	0.831	12.6
$KCdH_3$	221	5	41	686.4	0.533	12.3
Tc	194	4	10	213.7	0.808	12.2
Be_4NbRh	216	6	47	311.5	0.701	12.2
$LaRuH_2N$	123	5	16	337.0	0.690	12.0
RuO_2	136	6	0	444.4	0.601	11.7
NbB_2	191	3	0	394.7	0.625	11.5
ReTc	187	2	0	199.9	0.813	11.5
Ta	229	1	0	143.3	0.961	11.2
HfN	225	2	0	301.8	0.690	11.1

with an electron–phonon coupling constant of $\lambda = 0.99$ and an electronic logarithmic average of $\omega_{log} = 292$ K.

4.2. Hydrides

The remarkable increase in T_c observed in certain hydrogen-rich materials under high-pressure, such as sulfur hydride (H_3S)[7] and lanthanum hydride (LaH_{10}),[9] has attracted significant attention. These materials can exhibit T_c values soaring as high as 250 K, rivaling or even surpassing those of unconventional superconductors. This remarkable achievement has sparked enthusiasm within the scientific community. However, it is important to note that the practical application of these materials is hindered by the exceedingly high pressures (over 100–200 GPa) required to stabilize them. Our list of compounds with high-T_c at ambient pressure includes several hydride and hydrogen-containing materials.

The compound with the highest transition temperature among them is $LiPdH_2$. In the Li-Pd-H ternary phase diagrams, we have experimental knowledge of LiPdH[55] (a compound that is not superconducting above 4 K[55]), and Li_2PdH_2.[56] Regarding $LiPdH_2$, we find that it has a thermodynamically stable tetragonal phase. However, the compound with a high T_c is a trigonal allotrope that crystallizes in the delafossite structure, slightly higher in energy by 101 meV/atom with respect to the tetragonal phase.

The electron–phonon coupling in this compound primarily arises from interactions with high-energy optical phonons, predominantly falling within the range of 75 to 100 meV. The presence of these high-energy phonons is facilitated by the light mass of hydrogen. Consequently, the com pound exhibits a significant electron–phonon coupling constant of $\lambda = 0.98$ and an exceptionally high $\omega_{log} = 532$ K. These characteristics contribute to a high critical temperature of $T_c^{Eliashberg} = 43$ K.

The next hydride on our list is PdH, that exhibits a critical temperature of $T_c^{Eliashberg} = 37$ K. Palladium hydride is a well-known compound due to its anomalous isotope effect.[57–59] This effect manifests as an increase in T_c when hydrogen is replaced by deuterium or tritium. The anomalous behavior of PdH has been attributed to the presence of strong anharmonic effects,[60] which also lead to a substantial reduction in the predicted T_c values obtained using the harmonic approximation (utilized in this study) to approximately 5 K.[61]

ZrH_3 is a hypothetical compound situated 94 meV/atom above the convex hull, indicating its thermodynamic propensity to decompose into ZrH_2 and H_2. The compound discovered within our framework displays a tetragonal crystal structure, with zirconium atoms occupying the center of a cuboctahedron, while hydrogen atoms are located at the vertices. An intriguing feature of this material is that the DOS(E_F) is predominantly derived from the Zr states and these electrons are coupled with all phonon modes. Interestingly, a substantial contribution to the electron–phonon coupling constant of $\lambda = 0.97$ arises from the acoustic modes, which are exclusively associated with Zr vibrations, leading to a $T_c^{Eliashberg} = 24.9$ K.

Finally, we would like to highlight $KCdH_3$, a hydride perovskite compound (see **Figure 4**). In this case, the bottom of the conduction band falls below the Fermi level at the R point of the Brillouin

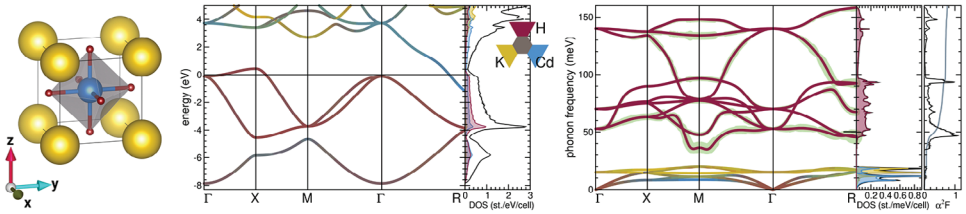

Figure 4. Left: View of the crystal structure of $KCdH_3$. The unit cell is shown in black, and the three lattice vectors are shown as arrows. K atoms are in orange, Cd atoms are in blue and H atoms are in red. Center: Atom resolved electronic band structure and density of states which, in the selected energy window, are dominated by Ti states. Right: Atom resolved phonon band structure and density of states. The width of the green shade behind the phonon band structure is proportional to the electron–phonon coupling of the corresponding phonon mode. In the rightmost panel are shown the Eliashberg function $\alpha^2F(\omega)$ and the integration curve of the electron–phonon coupling $\lambda(\omega)$. Note that the data depicted in this figure was obtained with material-specific convergence parameters (see Experimental Section), and is therefore slightly different from the values presented in Table 1.

zone, while the top conduction band is slightly above the Fermi level at the X point. Consequently, the Fermi surface exhibits both electron and hole pockets, with the Fermi level residing in a steep shoulder of the density of states. This material appears to have an interesting superconducting state, so we decided to study it with the fully anisotropic SCDFT approach (see Section 6). The hole pocket provides a Fermi surface sheet (see **Figure 5**) located near the X point and has mixed Cd-H character, carrying about 75% of the total DOS. The nearly spherical electron pocket arises from a pure Cd band and is located at the R-point contributing to about 25% of the DOS. However both Fermi surface pockets are quite small therefore the intraband electron–phonon coupling only comes from low q phonons. These have weak matrix elements and can not sustain superconductivity. Stronger coupling comes mostly from large q phonons via an interband scattering. Particularly important is the lowest hydrogen optical branch (rotations of the CdH_3 octahedra) of the phonons modes around the M and R points. The strong coupling is also responsible for an evident Kohn anomaly at the M point (see Figure 4). Clearly, owing to the different DOS, the interband scattering mechanism is particularly advantageous for the low DOS electron band that has a coupling about twice that of the hole pocket. It is crucial to note that this points to the fact that T_c is highly sensitive to the precise position of the Fermi level. In our most precise calculations using SCDFT, we estimate a critical temperature of 23.4 K, twice as large as the Eliashberg calculations in Table 1. The reason for this discrepancy is not only due to critical convergence aspects but also to the role of superconducting anisotropy that raises T_c by about 5K.

4.3. Intermetallics

We find a wealth of intermetallic materials at the top of our list. Among these, a significant number belong to well-known families of superconducting compounds, such as the A15 and C15 families, or are ternary generalizations of them.

Until the advent of the high-T_c ceramics in 1986, the superconductor with the highest known T_c belonged to the A15 family (Nb_3Ge with a T_c of 23.2 K). Although the binary phases of this family have been extensively investigated, the chemical space of ternary compounds is relatively unexplored. A15 compounds are cubic with the Cr_3Si structure type. There are several possibilities to generate ternary phases based on this prototype. For example, by varying the chemical species in the *2a* Wickoff positions one can generate materials such as Nb_6AlSi,[62] $AlSiMo_6$,[63] V_6GeOs,[64] etc. It is also possible to populate the *6c* positions with two different kinds of atoms as in V_2FeGe[65] or in $(NbV)_3Si_2$.[62]

In Table 1, we find several A15 compounds, such as Nb_3Zn with a T_c = 24.7 K, Cr_3Os with a T_c = 19.1 K, or Ti_3Te with a T_c = 16.3 K. We also find V_6CoSi that is a ternary A15 variant with a T_c = 16.2 K, and many more of those systems can be found in Table SIV in the Supporting Information. It is worth noting that we did not discover any high-T_c systems adopting the structure of V_2FeGe or $(NbV)_3S_2$.

We discuss in more detail Ti_3Te (see **Figure 6**) due to its unconventional chemical composition, specifically the inclusion of Te, a chemical element rarely found in high-T_c conventional superconductors. In this compound, the Fermi level occupies a relatively flat region of the DOS, predominantly composed of Ti states. The acoustic modes and the three lowest optical modes extend up to approximately 15.5 meV, with a significant hybridization between the vibrations of Ti and Te. As expected, the higher energy optical states primarily involve the lighter element, Ti. The electron–phonon coupling appears to be stronger at large **q** values, however all branches contribute significantly to the value of $\lambda = 1.0$, which, combined with ω_{log} = 187 K, results in a T_c = 14.8 K, as estimated from SCDFT. The estimation is not far from the 16.3 K obtained with isotropic Eliashberg theory and μ^*=0.10. However the SCDFT estimation accounts both for the anisotropy of the electron–phonon coupling, which actually increases T_c by about 2 K and uses the ab initio calculated electron–electron interaction which, as is often the case in transition metals, is quite strong (μ=0.4 and $\mu^* \simeq 0.15$). The superconducting gap on the Fermi surface is shown in Figure 5b. The gap distribution is peaked at a value of 2.4 meV featuring a large tail that reaches 3.1 meV on the cylindrical Fermi surface around the RM symmetry line.

The binary Laves phases, characterized by a cubic C15 structure like V_2Hf, exhibit a moderate T_c of approximately 10 K. Ternary variations[66] can be introduced through various approaches, resulting in compounds such as Mg_2SiNi_3 (possessing trigonal symmetry) or $MgCu_4Sn$ (exhibiting cubic symmetry). Some of these compounds have been found to superconducting, such as Mg_2SiIr_3 that displays a T_c of 7 K, or Li_2Si_3Ir that exhibits a T_c of 3.8 K.[67]

At the top of Table 1 with the cubic C15 structure we find $ZrTc_2$ with a T_c = 20.2 K, and a couple of ternary variants of this

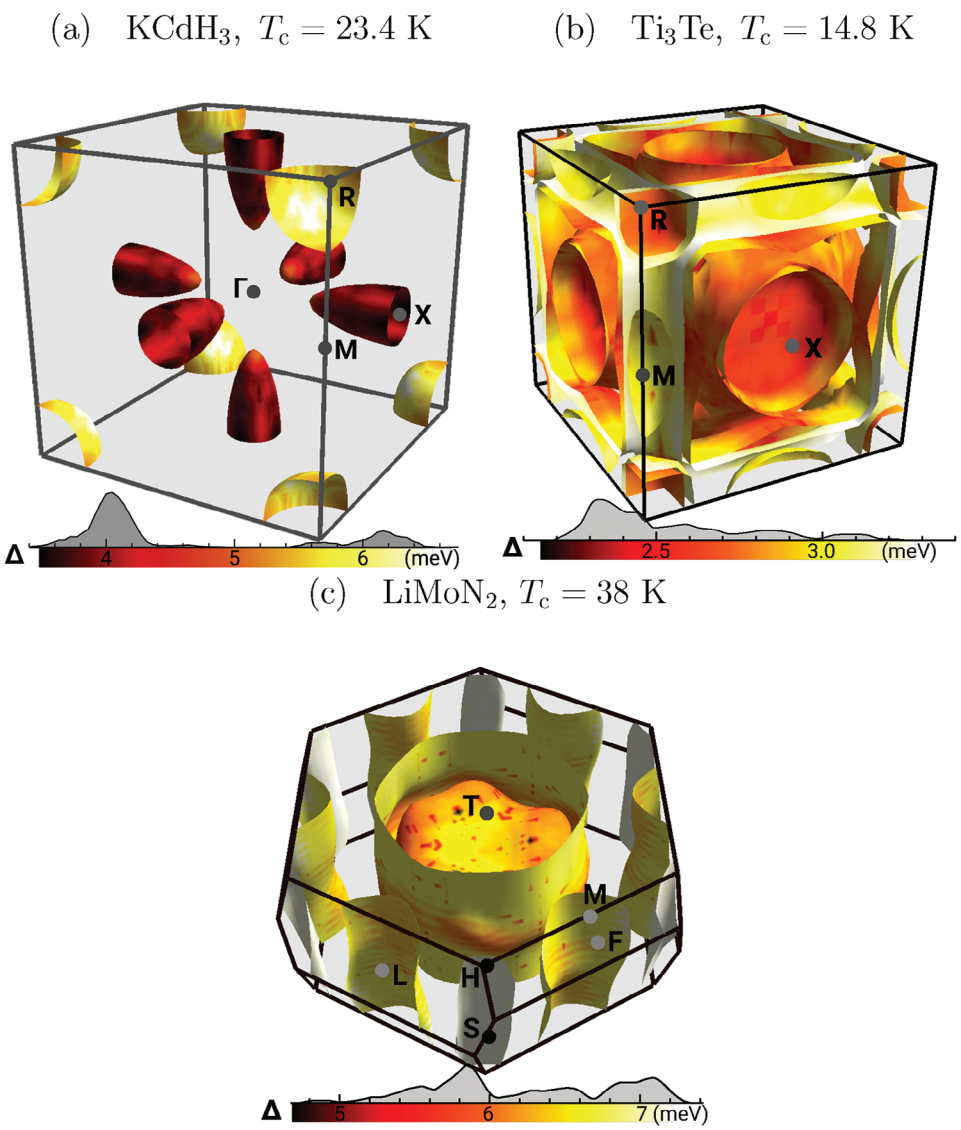

Figure 5. Fermi surfaces and gap distributions for three selected compounds. The coloring of the Fermi surface indicates the superconducting gap, as shown in the colorbar. The gray curves are gap distribution functions, defined as histograms of the superconducting gap at the Fermi energy. Calculations are performed at high precision using fully anisotropic SCDFT.

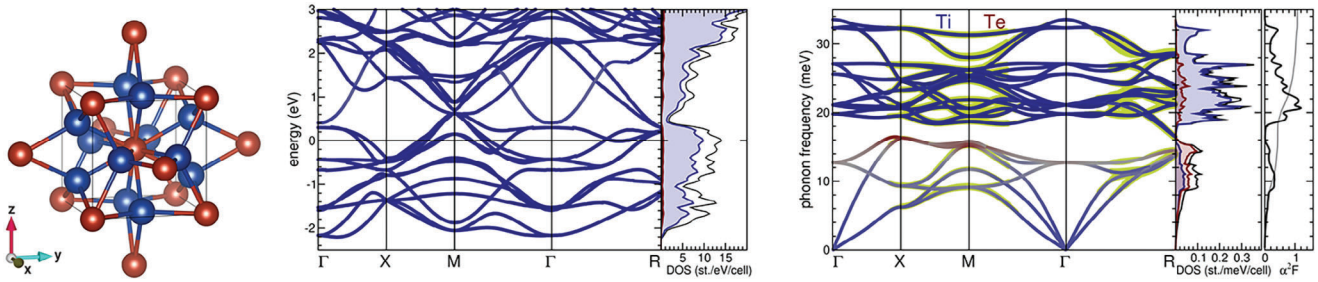

Figure 6. Left: View of the crystal structure of Ti_3Te. The unit cell is shown in black, and the three lattice vectors are shown as arrows. Ti atoms are in blue, Te atoms are in red. Center: Atom resolved electronic band structure and density of states which, in the selected energy window, are dominated by Ti states. Right: Atom resolved phonon band structure and density of states. The width of the green shade behind the phonon band structure is proportional to the electron–phonon coupling of the corresponding phonon mode. In the rightmost panel are shown the Eliashberg function $\alpha^2F(\omega)$ and the integration curve of the electron–phonon coupling $\lambda(\omega)$. Note that the data depicted in this figure was obtained with material-specific convergence parameters (see Experimental Section), and is therefore slightly different from the values presented in Table 1.

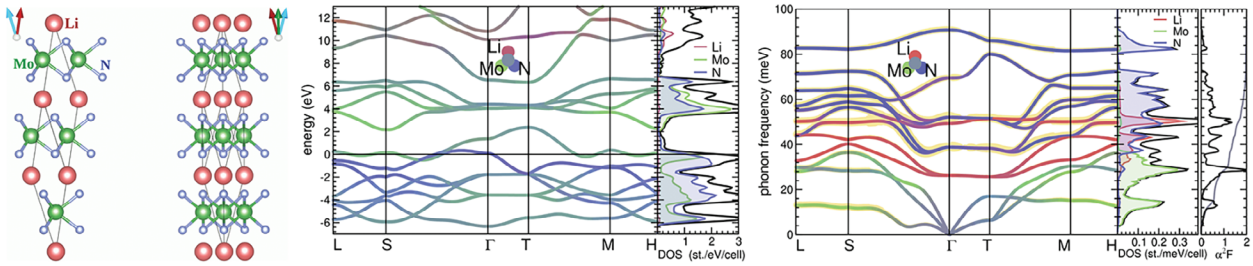

Figure 7. Left: Two views of the crystal structure of $LiMoN_2$. The unit cell is shown in black, and the three lattice vectors are shown as arrows. Li atoms are in red, Mo atoms are in green and N atoms in blue. This structure can be pictured as consisting of MoN_2 layers intercalated with Li. Center: Atom resolved electronic band structure and density of states. Right: Atom resolved phonon band structure and density of states. The width of the yellow shade behind the phonon band structure is proportional to the electron–phonon coupling of the corresponding phonon mode. In the rightmost panel are shown the Eliashberg function $\alpha^2F(\omega)$ and the integration curve of the electron–phonon coupling $\lambda(\omega)$. Note that the data depicted in this figure was obtained with material-specific convergence parameters (see Experimental Section), and is therefore slightly different from the values presented in Table 1.

structure such as Cr_4ReW with a $T_c = 24.3$ K, $TiNbV_4$ with a $T_c = 17.7$ K, or TiV_4Mo with a $T_c = 8.6$ K. Many more systems of this family can be found in Table SIV (Supporting Information). As an example, at the Fermi level of TiV_4Mo, we find states with mainly V character and much smaller Ti and Mo character. The Fermi level in this compound is on a shoulder of the DOS (while in $TiNbV_4$ it is essentially at the maximum of the peak). All phonon modes contribute to λ, with the largest contribution coming from the optical modes between 12.5 and 30.0 meV. This leads to a $\omega_{log} = 217.9$ K and $\lambda = 0.68$, yielding $T_c = 8.6$ K.

Finally, we would like to refer to a series of Ti–V compounds with rather high transition temperatures such as TiV_2 ($T_c = 24$ K), TiV ($T_c = 24$ K), and even the elementary substance V ($T_c = 24.9$ K). Unfortunately, these transition temperatures are certainly too high due to the neglect of spin fluctuations that are well-known to play an important role in Ti–V compounds.[68–70]

4.4. $LiMoN_2$

$LiMoN_2$ is a material that was overlooked in the search for superconductors. It was synthesized for the first time in 1992 by Elder and coauthors,[71] that were looking for nitride counterparts to the high-T_c ceramics, since N^{-III} is the ion most similar to O^{-II} with respect to size, polarizability, and electronegativity. This compound is a member of a family of layered nitrides that also includes $MgMoN_2$,[72] $MnMoN_2$ and $FeWN_2$,[73] $MnWN_2$, $NiWN_2$ and $CoWN_2$,[74] $LiWN_2$,[75] $CaTaN_2$,[76] $CaNbN_2$,[77] $NaTaN_2$, and $NaNbN_2$,[78] $SrZrN_2$, and $SrHfN_2$,[79] $SrTiN_2$,[80] $CuNbN_2$,[81] $LiSrGaN_2$,[82] $CrWN_2$,[83] $CuTaN_2$,[84] $BaZrN_2$,[85] $BaHfN_2$, $BaZr_{1-x}Hf_xN_2$.[86] From these, $CaTaN_2$ and $CaNbN_2$ are known to be superconductors, with T_c of ≈8.2 K and ≈14 K, respectively.[76,87] Note that these two compounds were also found by our methodology.

The structure of $LiMoN_2$ is depicted in the left panel of **Figure 7** and can be conceived as being composed of MoN_2 layers intercalated by Li. Interestingly, the MoN_2 layers are isostructural to the 2D transition-metal dichalcogenides, and can be obtained by replacing S→N in MoS_2. This leads, of course, to a charge destabilization, that is compensated by the extra electron from Li, leading to a metallic state. Of course, intercalating a divalent atom such as Mg leads to a semiconducting ground-state[72] where the two electrons fill the band formed by the lowest d_{z^2} orbitals.[88]

It is true that are striking structural similarities between $LiMoN_2$ and other intercalated compounds such as graphite (that when intercalated with Ca reaches transition temperatures above 10 K[89,90]). However, a closer look reveals that the separation between the opposing N sheets is smaller than the in-plane separation, suggesting that there is substantial direct bonding between opposing N layers.[91] Furthermore, an analysis of the electronic structure shows that $LiMoN_2$ is in fact a 3D metal.[87,91] As a 2D band structure (characteristic of the high-T_c ceramics or of MgB_2) was seen as an essential requirement for high-temperature superconductivity, $LiMoN_2$ was quickly dismissed after the initial synthesis as not being interesting.[87]

The electronic band-structure of $LiMoN_2$ is depicted in the center panel of Figure 7, together with the atom-resolved and total density of electronic states. We will keep the description of the electronic properties of $LiMoN_2$ brief, as they have already been discussed in Refs. [87, 91]. There are two bands crossing the Fermi level that are composed of d-states of Mo strongly hybridized with p-states of N. There is a large dispersion of the bands in the Γ–T direction, perpendicular to the basal planes, indicating the 3D character of the metal. We can see virtually no contribution of Li to the density-of-states indicating that these atoms are fully ionized. Finally, the Fermi level lies on a very large peak of the density-of-states, a fact that is often associated to superconductivity.

The phonon dispersion is plotted on the right panel of Figure 7. The material is stable dynamically, with three very different sound velocities showing the marked anisotropy of the compound. The three acoustical branches are essentially composed of Mo vibrations, as expected by the larger mass of Mo with respect to Li and N. The Li vibrations contribute mostly to the optical branches between 25 and 42 meV and have a dispersionless Einstein mode at 50 meV. The high-lying phonon branches until 95 meV are to a large extent composed of N vibrations. This is somewhat surprising in view of the mass difference between Li and N, and attests to the strength of covalent nitrogen bonds in the structure. Along the S-Γ line, we observe an incipient phonon instability corresponding to an in plane charge density wave distortion (CDW). An detailed analysis shows that the frequency of this CDW mode is numerically very unstable, with the mode softening at low electronic temperatures. The phonon frequencies remain, however, real in our most precise calculations.

Also in Figure 7, we show the Eliashberg function $\alpha^2F(\omega)$ and electron–phonon coupling constant $\lambda(\omega)$ of $LiMoN_2$. We see that almost all phonon branches (with the exception of the last ones) interact very strongly with the electronic states of Mo and N. As such the plot for $\alpha^2F(\omega)$ follows the features of the Mo and N phonon density-of-states until around 55 meV. Obviously, the Li vibrations do not couple to the electrons, as the bands at the Fermi level do not have any Li s-character. The final value of the electron–phonon coupling constant is $\lambda = 1.95$. This is a very large value, on par with the best conventional superconductors known to date, which are the high pressure hydrides (for which $\lambda \approx 2$). As a comparison MgB_2, the best phononic room pressure superconductor, has a coupling of $\lambda \approx 0.7$.

One should observe that the Fermi level is placed near a steep peak in the density of states, implying that the large coupling is, in part, caused by a large density of electronic states. Therefore, the value of λ can be misleading, as superconductivity arises from a broad region with a width of many hundredths of electron volts. Moreover, the coupling is unimportant unless associated with stiff phonon modes. In fact, large values of λ are often associated with soft-modes and lattice instabilities which do not necessarily lead to superconductivity. As seen in Figure 7 this is not the case for $LiMoN_2$ where the logarithmic average phonon frequency is ≈25 meV, which is small when compared with the hydrides (where it can be higher than 100 meV) and also smaller than for MgB_2 (about 60 meV), but still quite large as compared to most non-hydrogenic superconductors (13 meV in $NbSe_2$, 12 meV in Nb_3Sn, 6 meV in Pb, 16 meV in Nb, for example).

We predict a quite high critical temperature of approximately 40 K, similar to that of MgB_2. This value is significantly smaller than one would expect from a standard McMillan approach with $\mu^* = 0.10$, that predicts $T_c = 52$ K. The reason is in part to be ascribed to the strong variation of the density of states at the Fermi level, which causes a rapid drop of the electron–phonon coupling and, most importantly, a very strong Coulomb repulsion. The latter, similarly to the electron–phonon coupling, is increased by the high density of states at the Fermi level. However, it is weakly renormalized as the system has almost no states available between 1 and 3.5 eV above the Fermi level. A very large $\mu^* = 0.18$ would be needed, in an McMillan approach, to account for such effects.

We should point out that a Fermi energy located at a peak in the density of states suggests a possible incipient instability of the system, and most importantly also implies that the predicted value of T_c can depend considerably on the calculation parameters and approximations. For example, changing the functional to the standard Perdew-Burke-Ernzerhof approximation,[92] increases slightly $DOS(E_F)$, and causes a phonon softening, leading to an increase of T_c by almost 50%.

At zero temperature, the energy gap has values between 5 and 7 meV, with three gap regions. Anisotropy is remarkable but superconductivity is largely sustained by inter-band electron–phonon scattering, unlike the case of MgB_2 where coupling mostly occurs within Bσ orbitals. This leads to the fact that the three gaps have similar values. Nevertheless, anisotropy has an impact on T_c: calculations done assuming an isotropic coupling yield a slightly smaller T_c of 35 K.

An important question is if the high value of T_c predicted here can be realized experimentally. In our opinion this is mainly dependent on the quality of the experimental samples. The major problem seems to be related to disorder and incipient instabilities. The original synthesis resulted in a 15% concentration of Li_{Mo} anti-sites.[71] This can be understood as both Li and Mo sites are sixfold coordinated with N and that the cation–N distances are similar.[91] In order to understand if the formation of these defects is favourable, we computed their formation energy. We created a supercell of $LiMoN_2$ with 200 atoms (using the FIND_OPTIMAL_CELL_SHAPE routine from ASE[93]). This supercell was fully relaxed using a $1 \times 1 \times 1k$ −point grid, with all the remaining parameters kept identical to the calculations done in the manuscript. The total energy was then recalculated using a $3 \times 3 \times 3k$ −grid. We repeated this process for a supercell with the positions of one of the Li-Mo pair exchanged. From these, we obtained a formation energy of ≈ -0.3 eV, which indicates that the formation of these defects is indeed favorable from a thermodynamic point of view. This is in agreement with the experimental result that finds the spontaneous formation of anti-sites.[71] Of course, different synthesis processes may favor differently the formation of these (or other defects).

One can argue[91] that disorder would decrease $DOS(E_F)$, with a negative impact on superconductivity. On the other hand, it was found that up to 64% of the Li could be deintercalated from $LiMoN_2$.[71] This could be used to lower the position of the Fermi level, increasing the density-of-states at the Fermi level, and, in a first approximation, increasing the superconducting transition temperature. Furthermore, the fact that $LiMoN_2$ is close to a charge-density state can lead to structural deformations and consequent decrease of $DOS(E_F)$. Other problems could arise from the difficult in forming single-phase $LiMoN_2$ and the presence of secondary phases.[94]

5. Conclusion

We conducted an extensive investigation into conventional superconductivity by combining state-of-the-art calculations of the electron–phonon coupling with machine learning-accelerated high-throughput techniques. To achieve this, we created a comprehensive dataset comprising over 8250 ab initio electron–phonon calculations. This dataset represents a significant leap forward, as it is at least one order of magnitude larger than any previously available computational dataset for conventional superconductors. Furthermore, our calculations exhibit a good level of convergence, allowing us to identify intriguing superconducting materials and thoroughly examine the electron–phonon and superconducting properties across the entire spectrum of stable compounds.

Our dataset served as a foundation for training a machine learning model, leveraging compositional, structural, and ground-state properties as input features. Equipped with this powerful machine learning model, we explored a materials space encompassing approximately 200 000 metallic compounds. Our goal was to identify all superconducting compounds predicted to possess a T_c greater than 5 K. The model achieved a 70% success rate in this task. For comparison, in our initial dataset, only 10% of the materials fell within this range. Considering the full set of materials with calculated T_c greater than 5 K studied, 48%

of these were suggested by the machine learning model (50% if we consider materials with $T_c > 10$ K), while requiring seven times less calculations. We believe this attests the effectiveness of our approach.

Regarding the behavior observed across the materials space, we discovered that both ω_{log} and λ appear to follow a lognormal distribution. This distribution is asymmetric as these quantities cannot be negative. However, the underlying reasons for this distribution pattern remain currently unknown. This knowledge enabled us to estimate that the likelihood of encountering a metal with a λ value exceeding one, indicating a very strong electron–phonon coupling, is approximately 1%. Consequently, such compounds are rare occurrences within the materials space. Assuming uncorrelated lognormal distributions for ω_{log} and λ, we observe a superexponential distribution of T_c values. However the presence of large λ values often arises from soft phonons which lead to small ω_{log} values truncating the tail of the T_c distribution. In terms of probability to find superconductivity, our analysis suggests that within the set of stable, metallic and nonmagnetic materials, there is around a 0.4% chance of $T_c > 20$ K, and a 0.03% chance of superconductivity above 30 K. This finding aligns well with the long-held prejudice that conventional superconductivity is limited to approximately this temperature range. What we quantify here is that high T_c superconductivity with the phononic mechanism is so rare, in stable compounds, that an unbiased search is hopelessly inefficient and acceleration methods are necessary.

We observe a series of regularities in what concerns the chemistry of the materials with higher values of T_c. When considering metallic elements, Ti and V from the 4th row, as well as Zr, Nb, Mo, Tc, and Ru from the 5th row of the periodic table, display favorable characteristics for superconductivity. Additionally, many intermetallic compounds with high T_c values belong to well-established families, such as the A15 or C15 structures, or are ternary extensions of these. Despite an extensive exploration of numerous systems, we did not discover any compound of this nature surpassing a transition temperature of approximately 24 K. In fact, the most exceptional T_c values were found in compounds containing non-metallic elements, including H, N, O, and others. We identified 73 hydrides with T_c exceeding 5 K, as well as 45 nitrides, 31 carbides, and so on. It is worth emphasizing that our study also unveiled numerous superconducting compounds with unconventional chemical compositions or unique crystal structures.

The compound with the highest superconducting transition temperature in our study was the layered metal $LiMoN_2$ with $T_c \approx 38$ K. This value of T_c can be understood by the extreme electron–phonon coupling between the electrons participating in the very strong covalent bonds within the MoN_2 layers, with almost all N and Mo phonon modes contributing equally to a value of $\lambda = 1.9$. The material exhibits three different superconducting gaps, but, contrary to MgB_2, superconductivity seems to arise mainly from interband coupling. These results show that high-T_c superconductivity can exist in metallic layered nitride compounds and call for a detailed experimental analysis of these materials, and in particular of $LiMoN_2$.

An important effect that was neglected in the present study is anharmonicity. On the one hand anharmonicity can stabilize some compounds that in the harmonic approximation are dynamically unstable. In our workflow these are false negatives that we miss. On the other hand, anharmonic effects can alter considerably the phonon frequencies, leading to a change of the predicted values of T_c. The most widely known example of this is PdH, where anharmonicity decreases the transition temperature of almost 40 K to less than 10 K.[95] Clearly, these effects are strongest for compounds with light elements, and in particular for hydrides. In order to gain a comprehensive understanding of these effects, further investigations are necessary, such as employing advanced theoretical methods like the stochastic self-consistent harmonic approximation (SSCHA).[61,96] Unfortunately, these methods are very costly from the numerical point of view, and cannot be used in high-throughput studies.

One of the merits of employing the machine learning model is its capacity to probe hitherto uncharted territories in search of materials with high T_c. In this context this includes regions of material space with lower symmetry and larger cell sizes. We expect that the error of the machine is larger for this systems, that are absent from the training set. However, we also expect that including relatively few systems of this type in the training set —in the spirit of transfer learning— will suffice for the machine to provide reliable predictions. This suggests that targeting increasingly larger systems is an achievable goal. Another possible route to improve the reliability and efficiency of machine learning models is to add physically relevant descriptors, such as proposed, e.g., in Refs. [97, 98].

The synergy of machine-learning techniques and conventional density-functional based approaches holds great potential for a systematic exploration of the multinary phase diagram, enabling the search for superconducting compounds at high temperatures, and even room temperature. Furthermore, the availability of more data will inevitably make machine learning models more precise, in a virtuous cycle that will allow the community, in a near future, to investigate conventional superconducting properties of all possible stable materials, both at ambient as well as under pressure.

6. Experimental Section

Pseudopotentials: We used the Perdew-Burke-Ernzerhof for solids[99] (PBEsol) pseudopotentials from the PSEUDODOJO project,[100] specifically the stringent, scalar-relativistic norm-conserving set. This pseudopotential table has been systematically constructed and validated in a series of seven tests in crystalline environments, specifically the Δ-Gauge,[101] Δ′-Gauge,[102] GBRV-FCC, GBRV-BCC, GBRV-compound,[103] ghost-state detection, and phonons at the Γ-point.

The PSEUDODOJO set includes most chemical elements of the periodic table. Exceptions are lanthanides (although La and Lu are included) and actinides. We noticed severe convergence problems with Ir, that made us replace this pseudopotential by a previous version. For the cutoff energies, we used the maximum of PSEUDODOJO's high precision hint for the elements in a given material.

Electron–Phonon: All density-functional calculations were performed using the versions 6.8 and 7.1 of QUANTUM ESPRESSO[36,37] with the Perdew-Burke-Ernzerhof (PBE) for solids (PBEsol)[99] generalized gradient approximation.

Note that we did not use a *U* correction, that might be required for some correlated materials to obtain a correct electronic structure, nor we included the spin-orbit correction that might be relevant for some compounds with heavier atoms. We also did not include van der Waals corrections, that are however not expected to be relevant for the bulk compounds

studied here. As mentioned before, all materials with non-zero magnetic moments were removed from the dataset, so all calculations were performed without spin-polarization. For every material we re-optimized the structure that we obtained from the database.

Geometry optimizations were performed using uniform Γ-centered *k*-point grids with a density of 1500 *k*-points per reciprocal atom. If this results in an odd number of *k*-points in a given direction, the next even number was used instead. Convergence thresholds for energies, forces, and stresses were set to 1×10^{-8} a.u., 1×10^{-6} a.u., and 5×10^{-2} kbar, respectively. For the electron–phonon coupling we used a double-grid technique, with the same *k*-grid used in the lattice optimization as the coarse grid, and a *k*-grid quadrupled in each direction as the fine grid. For the *q*-sampling of the phonons we used half of the *k*-point grid described above. The double δ-integration to obtain the Eliashberg function was performed with a Methfessel–Paxton smearing of 0.05 Ry.

For the higher precision calculations, we repeated the previous steps by changing: i) the initial *k*-point grid density was set to 3000 *k*-points per reciprocal atom; ii) the *k*-grid used as the coarse grid was set to the double of the *k*-grid used for the geometry optimization. Our tests demonstrated that this adjustment is sufficient in most cases to replicate results obtained with manually converged grids. As an illustrative example let us consider MgB_2, which presents an extreme convergence challenge. In the normal precision setting, we obtained a T_c of 8.5 K, whereas the higher precision calculation yields a T_c of 16.7 K, in close proximity to the reported hand-converged values of 15.5 K[26] and 20 K.[104] Although the higher precision settings do not ensure convergence, it is much more probable that larger errors stem from other factors such as anharmonicity, charge density waves, anisotropy, multi-band effects, etc. Unfortunately, at the moment these aspects cannot be considered systematically in high-throughput studies like this one.

One of the main problems that we encountered was related to imaginary phonon frequencies. There are several aspects of this problem. First, compounds often exhibit imaginary frequencies at Γ due to the breaking of translation symmetry caused by numerical imprecision, either due to a too low energy cutoff or too few *k*-points, for example. To circumvent this problem, we accepted calculations where we encountered at most three imaginary frequencies at Γ if the maximum imaginary frequency was below $35i$ cm^{-1}. Otherwise the compound was discarded. We also encountered a few systems exhibiting spurious soft modes due to insufficient *k*-point sampling leading to instabilities. Finally, the *q* −point sampling may miss some phonon instabilities in undersampled regions of the Brillouin zone. All these problems lead to either false positive or false negative entries in the dataset. The former were eventually detected in the high precision step of the workflow. The false negatives, and in particular those compounds that the methodology labels as unstable, are unfortunately overlooked. While some of these false negatives could be stabilized by including, e.g., anharmonic effects, carrying out such computations becomes prohibitively costly, and we cannot at the moment afford the more complex calculations to bypass this issue.

Superconductivity: The values of

$$\lambda = 2 \int \frac{\alpha^2 F(\omega)}{\omega} \, d\omega \tag{1a}$$

$$\log(\omega_{\log}) = \frac{2}{\lambda} \int \frac{\log(\omega)}{\omega} \, \alpha^2 F(\omega) \, d\omega \tag{1b}$$

$$\omega_2^2 = \frac{2}{\lambda} \int \omega \, \alpha^2 F(\omega) \, d\omega \tag{1c}$$

where $\alpha^2 F(\omega)$ is the Eliashberg spectral function, are used to calculate the superconducting transition temperature using the McMillan formula[105,106]

$$T_c^{\text{McMillan}} = \frac{\omega_{\log}}{1.20} \exp\left[-1.04 \frac{1+\lambda}{\lambda - \mu^*(1+0.62\lambda)}\right] \tag{2}$$

and the Allen-Dynes modification[107] to it:

$$T_c^{\text{AD}} = f_1 f_2 T_c^{\text{McMillan}} \tag{3}$$

where the correction factors are

$$f_1 = \left\{1 + \left[\frac{\lambda}{2.46(1+3.8\mu^*)}\right]^{3/2}\right\}^{1/3} \tag{4a}$$

$$f_2 = 1 + \frac{\lambda^2(\omega_2/\omega_{\log} - 1)}{\lambda^2 + \left[1.82(1+6.3\mu^*)\omega_2/\omega_{\log}\right]^2} \tag{4b}$$

The function $\alpha^2 F(\omega)$ was also used to obtain T_c from the solution of the isotropic Eliashberg equations.

We took arbitrarily the value of $\mu^* = 0.10$ for all materials studied. We note that this procedure is well defined for the McMillan's and Allen-Dynes formulas, but not for the Eliashberg equations. Indeed, these depend on an extra parameter, the cutoff of the Coulomb interaction, and for which we took the (rather arbitrary) value of 0.5 eV. In general, we found that the transition temperature varies as $T_c^{\text{McMillan}} < T_c^{\text{Allen-Dynes}} < T_c^{\text{Eliashberg}}$, although the differences are in most cases not large. Note, however, that there are some outliers due to the presence of compounds with soft modes in DS-A.

DFT for Superconductors: The density of states of $LiMoN_2$ implies a strong energy variation of the gap, and the band structure indicates the likeliness of superconducting anisotropy (linked to the N and Mo orbital character at the Fermi level). For this reason, to study superconductivity we must adopt an anisotropic approach, accounting both for the anisotropy of the Fermi surface and the energy dependence of the electronic states. Presently, the only approach that can describe all these physical effects is superconducting density-functional theory[16,17] (SCDFT). In this theory, the only quantity we describe as isotropic is the Coulomb interaction, as tests have shown that its anisotropy has no significant effect in the results. We used the most recent SCDFT functional,[18] where the gap equation is solved for the Kohn-Sham gap, while the physical superconducting gap is computed from as a post processing step.

A strict energy cutoff of 104 Ry was used for $LiMoN_2$ and phonons and electron–phonon couplings were computed on a $12 \times 12 \times 12$ and $6 \times 6 \times 6$ grid for *k*- and *q*-points, respectively. These were interpolated to a set of 80 000 *k*-points on the Fermi surface, which was used for the SCDFT simulations.[108] For the calculation of the screened Coulomb interaction we used the RPA approximation for the screening function, which was computed on a $8 \times 8 \times 8$ *q*-grid.

The same framework was used to study $KCdH_3$ and $TiTe_3$. For $KCdH_3$ we converged the results using a 120 Ry cutoff, a $16 \times 16 \times 16$ ($8 \times 8 \times 8$) grid for *k* (*q*)-points for the calculation of the phonons and an $8 \times 8 \times 8$ *q*-grid for the screening function. For $TiTe_3$ we used a 120 Ry cutoff, an $8 \times 8 \times 8$ ($6 \times 6 \times 6$) grid for *k* (*q*)-points for the calculation of the phonons and a $6 \times 6 \times 6$ *q*-grid for the screening function.

Machine Learning: We calculated the Debye temperature (Θ_D) with the formalizm developed in Ref. [109] that provides a connection between this quantity and the elastic constants. To circumvent the calculation of the elastic constants, a relatively costly operation within DFT, we decided to use a machine learning model, namely the ALIGNN network.[41] For training, we employed the database of elastic constants presented in Ref. [110] from which we obtained a dataset of 10987 Debye temperatures. Due to the relationship between Θ_D and the elastic constants[109] we used the same hyperparameters as the best ALIGNN model trained for the bulk and shear modulus present in the MatBench repository.[111] The error obtained by the trained model in the test set was 25.3 K, while predicting the average of the train set (345.7 K) would result in an error of 133.2 K. A plot depicting the results of this machine can be found in the Supporting Information.

Looking at MatBench,[111] we see that for datasets of similar size to the superconducting data, the model that yields better results was MODNET.[40] We trained MODNET using as targets, simultaneously, λ, $\omega_{\log}$ and T_c with the error for each property weighted equally, as these were the choices yielding the best results. Hyperparameters were optimized using a grid search approach and fivefold cross-validation (see Supporting Information for details on the grid search and optimized parameters). For the final model we used the ensemble of the five models with smallest cross-validation error.

Supporting Information

Supporting Information is available from the Wiley Online Library or from the author.

Acknowledgements

T.F.T.C acknowledged financial support from FCT - Fundação para a Ciência e Tecnologia, Portugal (projects UIDB/04564/2020 and 2022.09975.PTDC) and the Laboratory for Advanced Computing at University of Coimbra for providing HPC resources that had contributed to the research results reported within this paper. M.A.L.M. acknowledged partial funding from Horizon Europe MSCA Doctoral network grant no.101073486, EUSpecLab, funded by the European Union, and from the Keele Foundation through the SuperC collaboration. M.A.L.M. gratefully acknowledged the Gauss Centre for Supercomputing e.V. (https://www.gauss-centre.eu) for funding this project by providing computing time on the GCS Supercomputer SuperMUC-NG at Leibniz Supercomputing Centre (https://www.lrz.de).

Open access funding enabled and organized by Projekt DEAL.

Author Contributions

T.F.T.C. and M.A.L.M. performed the high-throughput ab initio calculations. T.F.T.C trained the machine learning models. A.S. developed the Eliashberg solver and performed the SCDFT calculations. All authors contributed to designing the research, interpreting the results and writing of the manuscript.

Conflict of Interest

The authors declare no conflict of interest.

Data Availability Statement

The data that support the findings of this study are openly available in Materials Cloud at https://doi.org/10.24435/materialscloud:qv-bq , reference number 2023163.

Keywords

DFT calculations, electron–phonon calculations, high-throughput calculations, SCDFT, superconductivity

Received: July 18, 2023
Revised: November 3, 2023
Published online: December 2, 2023

[1] J. R. Hull, M. N. Wilson, L. Bottura, L. Rossi, M. A. Green, Y. Iwasa, S. Hahn, J.-L. Duchateau, S. S. Kalsi, in *Applied Superconductivity*, John Wiley & Sons, Ltd, Hoboken, New Jersey **2015**, pp. 403–602, Ch. 4.
[2] C. Yao, Y. Ma, *iScience* **2021**, *24*, 102541.
[3] J. G. Bednorz, K. A. Müller, *Z. Phys. B: Condens. Matter* **1986**, *64*, 189.
[4] J. Nagamatsu, T. Muranaka, Y. Zenitani, J. Akimitsu, *Nature (London)* **2001**, *410*, 63.
[5] Y. Kamihara, H. Hiramatsu, M. Hirano, R. Kawamura, H. Yanagi, T. Kamiya, H. Hosono, *J. Am. Chem. Soc.* **2006**, *128*, 10012.
[6] Y. Kamihara, T. Watanabe, M. Hirano, H. Hosono, *J. Am. Chem. Soc.* **2008**, *130*, 3296.
[7] A. P. Drozdov, M. I. Eremets, I. A. Troyan, V. Ksenofontov, S. I. Shylin, *Nature (London)* **2015**, *525*, 73.
[8] M. Somayazulu, M. Ahart, A. K. Mishra, Z. M. Geballe, M. Baldini, Y. Meng, V. V. Struzhkin, R. J. Hemley, *Phys. Rev. Lett.* **2019**, *122*, 027001.
[9] A. P. Drozdov, P. P. Kong, V. S. Minkov, S. P. Besedin, M. A. Kuzovnikov, S. Mozaffari, L. Balicas, F. F. Balakirev, D. E. Graf, V. B. Prakapenka, E. Greenberg, D. A. Knyazev, M. Tkacz, M. I. Eremets, *Nature (London)* **2019**, *569*, 528.
[10] J. A. Flores-Livas, L. Boeri, A. Sanna, G. Profeta, R. Arita, M. Eremets, *Phys. Rep.* **2020**, *856*, 1.
[11] J. Powell, in *Superconducting Machines and Devices: Large Systems Applications*, (Eds.: S. Foner, B. B. Schwartz), Springer US, Boston, MA, **1974**, pp. 1–85.
[12] A. Gurevich, *Nat. Mater.* **2011**, *10*, 255.
[13] H. Hosono, K. Tanabe, E. Takayama-Muromachi, H. Kageyama, S. Yamanaka, H. Kumakura, M. Nohara, H. Hiramatsu, S. Fujitsu, *Sci. Technol. Adv. Mater.* **2015**, *16*, 033503.
[14] L. Boeri, G. B. Bachelet, *J. Phys.: Condens. Matter* **2019**, *31*, 234002.
[15] F. Marsiglio, *Ann. Phys.* **2020**, *417*, 168102.
[16] M. Lüders, M. A. L. Marques, N. N. Lathiotakis, A. Floris, G. Profeta, L. Fast, A. Continenza, S. Massidda, E. K. U. Gross, *Phys. Rev. B* **2005**, *72*, 024545.
[17] M. A. L. Marques, M. Lüders, N. N. Lathiotakis, G. Profeta, A. Floris, L. Fast, A. Continenza, E. K. U. Gross, S. Massidda, *Phys. Rev. B* **2005**, *72*, 024546.
[18] A. Sanna, C. Pellegrini, E. K. U. Gross, *Phys. Rev. Lett.* **2020**, *125*, 057001.
[19] L. Boeri, R. Hennig, P. Hirschfeld, G. Profeta, A. Sanna, E. Zurek, W. E. Pickett, M. Amsler, R. Dias, M. I. Eremets, C. Heil, R. J. Hemley, H. Liu, Y. Ma, C. Pierleoni, A. N. Kolmogorov, N. Rybin, D. Novoselov, V. Anisimov, A. R. Oganov, C. J. Pickard, T. Bi, R. Arita, I. Errea, C. Pellegrini, R. Requist, E. K. U. Gross, E. R. Margine, S. R. Xie, Y. Quan, et al., *J. Phys.: Condens. Matter* **2022**, *34*, 183002.
[20] A. N. Kolmogorov, S. Shah, E. R. Margine, A. F. Bialon, T. Hammerschmidt, R. Drautz, *Phys. Rev. Lett.* **2010**, *105*, 217003.
[21] N. Geng, K. P. Hilleke, L. Zhu, X. Wang, T. A. Strobel, E. Zurek, *Journal of the American Chemical Society* **2023**, *145*, 1696.
[22] S. Saha, S. Di Cataldo, M. Amsler, W. von der Linden, B. Lilia, *Phys. Rev. B* **2020**, *102*, 024519.
[23] Y. Sun, J. Lv, Y. Xie, H. Liu, Y. Ma, *Phys. Rev. Lett.* **2019**, *123*, 097001.
[24] N. Hoffmann, T. F. T. Cerqueira, J. Schmidt, M. A. L. Marques, *npj Comput. Mater.* **2022**, *8*, 150.
[25] N. Hoffmann, T. F. T. Cerqueira, P. Borlido, A. Sanna, J. Schmidt, M. A. L. Marques, *npj Comput. Mater.* **2023**, *9*, https://doi.org/10.1038/s41524-023-01084-7.
[26] K. Choudhary, K. Garrity, *npj Comput. Mater.* **2022**, *8*, 244.
[27] D. Wines, K. Choudhary, A. J. Biacchi, K. F. Garrity, F. Tavazza, *Nano Lett.* **2023**, *23*, 969.
[28] C. C. Seegmiller, S. G. Baird, H. M. Sayeed, T. D. Sparks, *Comput. Mater. Sci.* **2023**, *228*, 112358.
[29] P. J. García-Nieto, E. García-Gonzalo, J. P. Paredes-Sánchez, *Neural Comput. Appl.* **2021**, *33*, 17131.
[30] V. Stanev, C. Oses, A. G. Kusne, E. Rodriguez, J. Paglione, S. Curtarolo, I. Takeuchi, *npj Comput. Mater.* **2018**, *4*, https://doi.org/10.1038/s41524-018-0085-8.

[31] H. Hosono, K. Tanabe, E. Takayama-Muromachi, H. Kageyama, S. Yamanaka, H. Kumakura, M. Nohara, H. Hiramatsu, S. Fujitsu, *Sci. Technol. Adv. Mater.* **2015**, *16*, 033503.
[32] T. Sommer, R. Willa, J. Schmalian, P. Friederich, *Sci. Data* **2023**, *10*, 816.
[33] J. Schmidt, L. Pettersson, C. Verdozzi, S. Botti, M. A. L. Marques, *Sci. Adv.* **2021**, *7*, eabi7948.
[34] J. Schmidt, N. Hoffmann, H.-C. Wang, P. Borlido, P. J. M. A. Carriço, T. F. T. Cerqueira, S. Botti, M. A. L. Marques, *Adv. Mater.* **2023**, *35*, 2210788.
[35] S. Baroni, P. Giannozzi, A. Testa, *Phys. Rev. Lett.* **1987**, *58*, 1861.
[36] P. Giannozzi, O. Andreussi, T. Brumme, O. Bunau, M. B. Nardelli, M. Calandra, R. Car, C. Cavazzoni, D. Ceresoli, M. Cococcioni, N. Colonna, I. Carnimeo, A. D. Corso, S. de Gironcoli, P. Delugas, R. A. DiStasio, A. Ferretti, A. Floris, G. Fratesi, G. Fugallo, R. Gebauer, U. Gerstmann, F. Giustino, T. Gorni, J. Jia, M. Kawamura, H.-Y. Ko, A. Kokalj, E. Küçükbenli, M. Lazzeri, et al., *J. Phys.: Condens. Matter* **2017**, *29*, 465901.
[37] P. Giannozzi, S. Baroni, N. Bonini, M. Calandra, R. Car, C. Cavazzoni, D. Ceresoli, G. L. Chiarotti, M. Cococcioni, I. Dabo, A. D. Corso, S. de Gironcoli, S. Fabris, G. Fratesi, R. Gebauer, U. Gerstmann, C. Gougoussis, A. Kokalj, M. Lazzeri, L. Martin-Samos, N. Marzari, F. Mauri, R. Mazzarello, S. Paolini, A. Pasquarello, L. Paulatto, C. Sbraccia, S. Scandolo, G. Sclauzero, A. P. Seitsonen, et al., *J. Phys.: Condens. Matter* **2009**, *21*, 395502.
[38] J. P. Perdew, Y. Wang, *Phys. Rev. B* **1992**, *45*, 13244.
[39] P. B. Allen, R. C. Dynes, *Phys. Rev. B* **1975**, *12*, 905.
[40] P.-P. D. Breuck, G. Hautier, G.-M. Rignanese, *npj Comput. Mater.* **2021**, *7*, 83.
[41] K. Choudhary, B. DeCost, *npj Comput. Mater.* **2021**, *7*, 185.
[42] J. M. An, W. E. Pickett, *Phys. Rev. Lett.* **2001**, *86*, 4366.
[43] P. Virtanen, R. Gommers, T. E. Oliphant, M. Haberland, T. Reddy, D. Cournapeau, E. Burovski, P. Peterson, W. Weckesser, J. Bright, S. J. van der Walt, M. Brett, J. Wilson, K. J. Millman, N. Mayorov, A. R. J. Nelson, E. Jones, R. Kern, E. Larson, C. J. Carey, İ. Polat, Y. Feng, E. W. Moore, J. VanderPlas, D. Laxalde, J. Perktold, R. Cimrman, I. Henriksen, E. A. Quintero, C. R. Harris, et al., *Nat. Methods* **2020**, *17*, 261.
[44] J. Schmidt, H.-C. Wang, T. F. T. Cerqueira, S. Botti, M. A. L. Marques, *Sci. Data* **2022**, *9*, 64.
[45] Y. Katsura, A. Yamamoto, H. Ogino, S. Horii, J. ichi Shimoyama, K. Kishio, H. Takagi, *Phys. C* **2010**, *470*, S633.
[46] A. I. Gusev, A. A. Rempel, *Phys. Status Solidi B* **1989**, *151*, 211.
[47] C. Buzea, T. Yamashita, *Supercond. Sci. Technol.* **2001**, *14*, R115.
[48] J. E. van Nostrand, J. D. Albrecht, R. Cortez, K. D. Leedy, B. Johnson, M. J. O'keefe, *J. Electron. Mater.* **2005**, *34*, 1349.
[49] M. Maunaye, J. Guyader, Y. Laurent, J. Lang, *Bull. Soc. Fr. Mineral. Cristallogr.* **1971**, *94*, 347.
[50] R. Marchand, P. L'Haridon, Y. Laurent, *J. Solid State Chem.* **1982**, *43*, 126.
[51] K. Landskron, S. Schmid, W. Schnick, *Z. Anorg. Allg. Chem.* **2001**, *627*, 2469.
[52] P. Eckerlin, *Z. Anorg. Allg. Chem.* **1967**, *353*, 225.
[53] J. David, Y. Laurent, J. Lang, *Bull. Soc. Fr. Mineral. Cristallogr.* **1970**, *93*, 153.
[54] M. Wintenberger, M. Maunaye, Y. Laurent, *Mater. Res. Bull.* **1973**, *8*, 1049.
[55] D. Noréus, O. Rapp, *Phys. Rev. B* **1990**, *42*, 10730.
[56] K. Kadir, D. Noréus, *Z. Phys. Chem.* **1989**, *163*, 231.
[57] B. Stritzker, W. Buckel, *Z. Phys. A: Hadrons Nucl.* **1972**, *257*, 1.
[58] J. E. Schirber, C. J. M. Northrup, *Phys. Rev. B* **1974**, *10*, 3818.
[59] J. Schirber, J. Mintz, W. Wall, *Solid State Commun.* **1984**, *52*, 837.
[60] A. Karakozov, E. Maksimov, *Zh. Eskp. Teor. Fiz* **1978**, *74*, 681.
[61] I. Errea, M. Calandra, F. Mauri, *Phys. Rev. Lett.* **2013**, *111*, 177002.
[62] P. Muller, *Z. Metallkde.* **1977**, *68*, 421.
[63] C. Brukl, H. Nowotny, F. Benesovsky, *Monatsh. Chem.* **1961**, *92*, 967.
[64] A. Pavlyuchenko, *Phys. Solid State* **1978**, *20*, 2090.
[65] K. Kanematsu, *Trans. Jpn. Inst. Met.* **1986**, *27*, 225.
[66] N. L. Gulay, Y. M. Kalychak, R. Pöttgen, *Z. Anorg. Allg. Chem.* **2021**, *647*, 75.
[67] K. Kudo, H. Hiiragi, T. Honda, K. Fujimura, H. Idei, M. Nohara, *J. Phys. Soc. Jpn.* **2020**, *89*, 013701.
[68] M. Matin, L. S. S. Chandra, S. K. Pandey, M. K. Chattopadhyay, S. B. Roy, *Eur. Phys. J. B* **2014**, *87*, 131.
[69] M. Matin, L. S. Chandra, R. Meena, M. Chattopadhyay, A. Sinha, M. Singh, S. Roy, *Phys. B* **2014**, *436*, 20.
[70] S. K. Bose, *J. Phys.: Condens. Matter* **2008**, *21*, 025602.
[71] S. Elder, L. H. Doerrer, F. DiSalvo, J. Parise, D. Guyomard, J. Tarascon, *Chem. Mater.* **1992**, *4*, 928.
[72] R. Verrelli, M. E. Arroyo-de Dompablo, D. Tchitchekova, A. P. Black, C. Frontera, A. Fuertes, M. R. Palacín, *Phys. Chem. Chem. Phys.* **2017**, *19*, 26435.
[73] D. S. Bem, C. M. Lampe-Önnerud, H. P. Olsen, H.-C. zur Loye, *Inorg. Chem.* **1996**, *35*, 581.
[74] P. S. Herle, N. Vasanthacharya, M. Hegde, J. Gopalakrishnan, *J. Alloys Compd.* **1995**, *217*, 22.
[75] P. S. Herle, M. Hegde, N. Vasanthacharya, J. Gopalakrishnan, G. Subbanna, *J. Solid State Chem.* **1994**, *112*, 208.
[76] V. Balbarin, R. Van Dover, F. DiSalvo, *J. Phys. Chem. Solids* **1996**, *57*, 1919.
[77] T. Brokamp, Ph.D. thesis, Universität Dortmund **1991**.
[78] R. Niewa, H. Jacobs, *Chem. Rev.* **1996**, *96*, 2053.
[79] D. Gregory, M. Barker, P. Edwards, D. Siddons, *Inorg. Chem.* **1996**, *35*, 7608.
[80] G. Farault, R. Gautier, C. F. Baker, A. Bowman, D. H. Gregory, *Chem. Mater.* **2003**, *15*, 3922.
[81] A. Zakutayev, A. J. Allen, X. Zhang, J. Vidal, Z. Cui, S. Lany, M. Yang, F. J. DiSalvo, D. S. Ginley, *Chem. Mater.* **2014**, *26*, 4970.
[82] D. G. Park, Z. A. Gál, F. J. DiSalvo, *J. Alloys Compd.* **2003**, *353*, 107.
[83] K. Weil, P. Kumta, *J. Solid State Chem.* **1997**, *128*, 185.
[84] U. Zachwieja, H. Jacobs, *Eur. J. Solid State Inorg. Chem.* **1991**, *28*, 1055.
[85] O. Seeger, M. Hofmann, J. Strähle, J. Laval, B. Frit, *Z. Anorg. Allg. Chem.* **1994**, *620*, 2008.
[86] D. Gregory, M. Barker, P. Edwards, M. Slaski, D. Siddons, *J. Solid State Chem.* **1998**, *137*, 62.
[87] J. M. Oliva, R. Weht, P. Ordejón, E. Canadell, *Phys. Rev. B* **2000**, *62*, 1512.
[88] L. F. Mattheiss, *Phys. Rev. Lett.* **1973**, *30*, 784.
[89] T. E. Weller, M. Ellerby, S. S. Saxena, R. P. Smith, N. T. Skipper, *Nat. Phys.* **2005**, *1*, 39.
[90] R. P. Smith, T. E. Weller, C. A. Howard, M. P. Dean, K. C. Rahnejat, S. S. Saxena, M. Ellerby, *Phys. C* **2015**, *514*, 50.
[91] D. Singh, *Phys. Rev. B* **1992**, *46*, 9332.
[92] J. P. Perdew, K. Burke, M. Ernzerhof, *Phys. Rev. Lett.* **1996**, *77*, 3865.
[93] A. H. Larsen, J. J. Mortensen, J. Blomqvist, I. E. Castelli, R. Christensen, M. Dułak, J. Friis, M. N. Groves, B. Hammer, C. Hargus, E. D. Hermes, P. C. Jennings, P. B. Jensen, J. Kermode, J. R. Kitchin, E. L. Kolsbjerg, J. Kubal, K. Kaasbjerg, S. Lysgaard, J. B. Maronsson, T. Maxson, T. Olsen, L. Pastewka, A. Peterson, C. Rostgaard, J. Schiøtz, O. Schütt, M. Strange, K. S. Thygesen, T. Vegge, et al., *J. Phys. Condens. Matter* **2017**, *29*, 273002.

[94] S. M. Hunter, Ph.D. thesis, University of Glasgow **2008**.
[95] I. Errea, M. Calandra, F. Mauri, *Phys. Rev. Lett.* **2013**, *111*, https://doi.org/10.1103/physrevlett.111.177002.
[96] L. Monacelli, R. Bianco, M. Cherubini, M. Calandra, I. Errea, F. Mauri, *J. Phys.: Condens. Matter* **2021**, *33*, 363001.
[97] Y. Sun, F. Zhang, C.-Z. Wang, K.-M. Ho, I. I. Mazin, V. Antropov, *Phys. Rev. Mater.* **2022**, *6*, https://doi.org/10.1103/physrevmaterials.6.074801.
[98] F. Belli, T. Novoa, J. Contreras-García, I. Errea, *Nat. Commun.* **2021**, *12*, https://doi.org/10.1038/s41467-021-25687-0.
[99] J. P. Perdew, A. Ruzsinszky, G. I. Csonka, O. A. Vydrov, G. E. Scuseria, L. A. Constantin, X. Zhou, K. Burke, *Phys. Rev. Lett.* **2008**, *100*, 136406.
[100] M. van Setten, M. Giantomassi, E. Bousquet, M. Verstraete, D. Hamann, X. Gonze, G.-M. Rignanese, *Comput. Phys. Commun.* **2018**, *226*, 39.
[101] K. Lejaeghere, V. V. Speybroeck, G. V. Oost, S. Cottenier, *Crit. Rev. Solid State Mater. Sci.* **2013**, *39*, 1.
[102] F. Jollet, M. Torrent, N. Holzwarth, *Comput. Phys. Commun.* **2014**, *185*, 1246.
[103] K. F. Garrity, J. W. Bennett, K. M. Rabe, D. Vanderbilt, *Comput. Mater. Sci.* **2014**, *81*, 446.
[104] A. Floris, G. Profeta, N. N. Lathiotakis, M. Lüders, M. A. L. Marques, C. Franchini, E. K. U. Gross, A. Continenza, S. Massidda, *Phys. Rev. Lett.* **2005**, *94*, https://doi.org/10.1103/physrevlett.94.037004.
[105] W. L. McMillan, *Phys. Rev.* **1968**, *167*, 331.
[106] R. Dynes, *Solid State Commun.* **1972**, *10*, 615.
[107] P. B. Allen, R. C. Dynes, *Phys. Rev. B* **1975**, *12*, 905.
[108] A. Sanna, C. Pellegrini, E. Liebhaber, K. Rossnagel, K. J. Franke, E. K. U. Gross, *npj Quantum Mater.* **2022**, *7*, 6.
[109] O. L. Anderson, *J. Phys. Chem. Solids* **1963**, *24*, 909.
[110] M. de Jong, W. Chen, T. Angsten, A. Jain, R. Notestine, A. Gamst, M. Sluiter, C. K. Ande, S. van der Zwaag, J. J. Plata, C. Toher, S. Curtarolo, G. Ceder, K. A. Persson, M. Asta, *Sci. Data* **2015**, *2*, 150009.
[111] A. Dunn, Q. Wang, A. Ganose, D. Dopp, A. Jain, *npj Comput. Mater.* **2020**, *6*, 138.